Mon. Not. R. Astron. Soc. **000**, 000–000 (0000) Printed 10 May 2016 (MN LATEX style file v2.2)

Physical and chemical properties of Red MSX Sources in the southern sky: HII regions

Naiping Yu[1,2⋆], Jun-Jie Wang[1,2] and Nan Li[1,2⋆†]
[1]*National Astronomical Observatories, Chinese Academy of Sciences, Beijing 100012, China*
[2]*NAOC-TU Joint Center for Astrophysics, Lhasa 850000, China*

10 May 2016

arXiv:1605.02092v1 [astro-ph.GA] 5 May 2016

ABSTRACT

We have studied the physical and chemical properties of 18 southern Red MSX Sources (RMSs), using archival data taken from the APEX Telescope Large Area Survey of the Galaxy (ATLASGAL), the Australia Telescope Compact Array (ATCA), and the Millimeter Astronomy Legacy Team Survey at 90 GHz (MALT90). Most of our sources have simple cometary/unresolved radio emissions at 4.8GHz and/or 8.6GHz. The large number of Lyman continuum fluxes (N_L) indicates they are probably massive O or early B type star formation regions. Archival IRAS infrared data is used to estimate the dust temperature, which is about 30 K of our sources. Then the H_2 column densities and the volume-averaged H_2 number densities are estimated using the 870 μm dust emissions. Large scale infall and ionized accretions may be occurring in G345.4881+00.3148. We also attempt to characterize the chemical properties of these RMSs through molecular line (N_2H^+ (1-0) and HCO^+ (1-0)) observations. Most of the detected N_2H^+ and HCO^+ emissions match well with the dust emission, implying a close link to their chemical evolution in the RMSs. We found the abundance of N_2H^+ is one order of magnitude lower than that in other surveys of IRDCs, and a positive correlation between the abundances of N_2H^+ and HCO^+. The fractional abundance of N_2H^+ with respect to H_2 seems to decrease as a function of N_L. These observed trends could be interpreted as an indication of enhanced destruction of N_2H^+, either by CO or through dissociative recombination with electrons produced by central UV photons.

Key words: stars: formation - ISM: HII regions - ISM: abundances - ISM: molecules - ratio lines

1 INTRODUCTION

One of the key challenges in stellar astrophysics is to understand the formation of massive stars and their role in the evolution of the universe. A lot of research has been done in astrophysics in the last two decades and considerable progress has been seen in the understanding of massive star formation (Zinnecker & Yorke 2007). Even though their short lives and rare sources, massive stars play a major role in determining physical, chemical and morphological structures of galaxies through ionizing radiation, heating of dust and expansions of their HII regions. These processes may also trigger next generation of star formation by compressing neighboring molecular clouds to the point of gravitational instability. It is generally accepted that massive stars evolve through starless cores in infrared dark clouds (IRDCs) to hot molecular cores (HMCs; e.g. Kurtz et al. 2000). Then substantial UV photons and ionized stellar winds rapidly ionize the surrounding hydrogen, forming a hyper-compact HII region (HCHII) or ultra-compact HII region (UCHII). The final stages are compact and classical HII regions. However, many questions are still unclear: whether accretion could be halted by the strong outward radiation and thermal pressure? Does it continue in an ionized form? Does it continue through a molecular or ionized disk? Chemical composition of molecular gas is thought to evolve due to the physical changes that occur during the star formation process. As material collapses and gets ionized by central young stars, densities and temperature rise, leading to the production and destruction of different molecular species. Multi-wavelength observations are vital to our understanding of the physical and chemical conditions where massive star formation occurs.

IRDCs provide us with the possibility of investigating the subsequent early stages of high mass star formation,

⋆ E-mail: yunaiping09@mails.gucas.ac.cn
†

and a lot of research has also been done to investigate their physical and chemical properties (e.g. Vasyunina et al. 2009; Vasyunina et al. 2011; Hoq et al. 2013; Liu et al. 2013; Miettinen 2014). In order to characterize the different evolutionary stages of IRDCs, Chambers et al. (2009) proposed an evolutionary sequence in which "quiescent" clumps evolve into "intermediate", "active" and "red" clumps, based on the Spitzer observations. Sanhueza et al. (2012) and Hoq et al. (2013) characterize the chemical properties of a sample of IRDCs using the data of MALT90. Correlations and anti-correlations between molecular abundances and the evolutionary stages have been found. These studies suggest chemical processes in high-mass star formations may differ from their low-mass counterparts, as their temperature, densities and UV fluxes are very different from each other. Establishing the chemical properties of massive star formation requires that large surveys be conducted.

In this paper, we describe our physical and chemical studies of RMSs (mainly HII regions) and compare our results with previous IRDCs observations. The RMS survey was conceived at Leeds to systematically search the entire Galaxy for MYSOs, by comparing the colors of sources from the Midcourse Space Experiment (MSX) and Two-Micron All-Sky Survey (2MASS) point sources (Lumsden et al. 2002). The RMS survey is an ongoing multi-wavelength observational programme (e.g. Urquhart et al. 2007a; Urquhart et al. 2007b) and will provide us with the largest MYSO sample for statistical studies. We have analyzed 18 RMSs in the southern sky using archival data from ATLASGAL, ATCA and MALT90. N_2H^+ and HCO^+ are both good tracers of dense gases, as their critical density $n_{crit} > 10^5$ cm^{-3}. N_2H^+ is more resistent to freeze-out on grains than the carbon-bearing species (Hirota et al. 1998). So it is an excellent tracer of cold and dense molecular clouds. In star formation regions, it is primarily formed through the gas-phase reaction $H_3^+ + N_2 \rightarrow N_2H^+ + H_2$, and destroyed by CO molecules in the gas-phase through $N_2H^+ + CO \rightarrow HCO^+ + N_2$. It can also be destroyed in the electron recombination: $N_2H^+ + e^- \rightarrow N_2 + H$ or $NH + N$ (e.g. Dislaire et al. 2012; Vigren et al. 2012). In dense molecular clouds, HCO^+ is mainly formed through the gas-phase ion-neutral reaction $H_3^+ + CO \rightarrow HCO^+ + H_2$ (e.g. Herbst & Klemperer 1973). The HCO^+ abundance can also be increased in regions where shocks are generated. In chemical models of low mass star formation, a relative enhancement of N_2H^+ and a depletion of HCO^+ abundances are expected in the cold prestellar phase, as CO is thought to be depleted in starless cores (e.g. Lee et al. 2003, 2004; Bergin & Tafalla 2007). When the central star evolves, the gas gets warmer and CO should be evaporated from the dust grains if the dust temperature exceeds about $\sim$ 20 K (Tobin et al. 2013). Thus the HCO^+ abundance should increase while the N_2H^+ abundance drops.

2 DATA SETS AND SOURCE SELECTIONS

The MALT90 is a large international project aimed at characterizing the sites within our Galaxy where high-mass stars will form. The target clumps are selected from the 870 μm ATLASGAL to host the early stages of high-mass star formation and include pre-stellar clumps, protostellar clumps, and HII regions. Exploiting the unique broad frequency range and fast-mapping capabilities of the Mopra 22-m telescope, MALT90 maps 16 emission lines simultaneously at frequencies near 90 GHz. These molecular lines will probe the physical, chemical and evolutionary states of dense high-mass star-forming cores. The survey covers a Galactic longitude range of $\sim$ -60 to $\sim$ 15° and Galactic latitude range of -1 to +1 °. The observations were carried out with the newly upgraded Mopra Spectrometer (MOPS). The full 8 GHz bandwidth of MOPS was split into 16 zoom bands of 138 MHz each providing a velocity resolution of $\sim$ 0.11 km s^{-1}. The angular resolution of Mopra is about 38 arcsec, with beam efficiency between 0.49 at 86 GHz and 0.42 at 115 GHz (Ladd et al. 2005). The mapping sizes are $3'.4 \times 3'.4$ with $9''$ spacing between adjacent rows. The MALT90 data includes (l, b, v) data cubes and (l, b) moment and error maps, and is publicly available from the MALT90 Home Page[1]. More information about this survey can be found in Foster et al. (2011) and Hoq et al. (2013). The data processing was conducted using CLASS (Continuum and Line Analysis Single-Disk Software) and GreG (Grenoble Graphic) software packages.

The ATLASGAL is the first systematic survey of the inner Galactic plane in the sub-millimeter. The observations were carried out with the Large APEX Bolometer Camera (LABOCA), an array of 295 bolometers observing at 870 μm (Contreras et al. 2013). The aim of this survey is to obtain a complete census of cold dusty clumps in the Galaxy, and to study their distributions across the Galaxy. The half-power beam width (HPBW) of the telescope is $18.''6$ ($\sim$ 0.22 pc at 2.4 kpc) at the frequency used. The total field of view (FoV) of LABOCA is $11.'4$. The instrument and its observing modes are described in Siringo et al. (2009). And the data reduction is described in Contreras et al. (2013).

In order to choose a genuine sample of MYSOs from the RMSs, Urquhart et al. (2007a) have completed the 5-GHz observations of 892 RMS sources in the southern sky using the ATCA. According to the observations, they divided these sources into three groups: real MYSO candidates, HII regions (UCHII and HCHII) and others such as evolved stars and planetary nebulae (PNe). The radio continuum emissions allow us to derive the expected spectral type of the exciting stars. Assuming an electron of $T_e = 10^4$ K, the number of UV ionizing photons needed to keep an HII region ionized is given as (Chaisson 1976):

$$N_L = 7.6 \times 10^{46} s^{-1} (\frac{S_\nu}{Jy})(\frac{D}{kpc})^2 (\frac{\nu}{GHz})^{0.1} (\frac{T_e}{10^4 K})^{-0.45} \quad (1)$$

The large number of Lyman continuum fluxes (listed in Table 1, column 7) indicates they are probably massive O or early B type star formation regions.

In order to study physical and chemical properties in massive star formation regions, we selected 18 sources from the RMS survey by applying the following criteria: (i)According to the observations of ATCA (Urquhart et al. 2007a), sources should have simple spherical/unresolved/shell-like/cometary radio emissions. (ii)The N_2H^+ and HCO^+ emissions of our sources should be detected by MALT90, and the local standard of rest (LSR)

[1] See http://atoa.atnf.csiro.au/MALT90

Table 1. List of our sources.

RMS name	RA (J2000)	Dec. (J2000)	V_{lsr} (km s^{-1})	D (kpc)	$S_{4.8GHz}$[a] (mJy)	$\log(N_L)$ (S^{-1})
G330.2838+00.4933	16:03:43.28	-51:51:45.6	-94.2	5.32±0.06	44.9	47.05±0.05
G331.4181−00.3546	16:12:50.24	-51:43:28.5	-63.2	3.90±0.05	83.9	46.78±0.06
G332.2944−00.0962	16:15:45.83	-50:56:02.4	-48.7	3.64±0.03	175.6	47.30±0.04
G332.5438−00.1277	16:17:02.33	-50:47:03.3	-47.1	3.64±0.06	42.2	46.69±0.07
G332.8256−00.5498A	16:20:11.06	-50:53:16.2	-58.1	3.64±0.05	1259.0	48.16±0.07
G333.3401−00.1273	16:20:37.00	-50:13:32.7	-59.7	3.64±0.03	3.3	45.58±0.04
G337.0047+00.3226	16:34:04.73	-47:16:29.2	-62.4	11.43±0.05	249.3	48.46±0.02
G337.4032−00.4037	16:38:50.44	-47:28:03.0	-40.0	3.14±0.04	90.3	46.89±0.06
G337.7091+00.0932A	16:37:51.80	-46:54:33.4	-75.9	10.98±0.04	144.9	48.19±0.02
G337.8442−00.3748	16:40:26.68	-47:07:13.1	-39.9	3.06±0.06	11.1	45.95±0.09
G339.1052+00.1490	16:42:59.58	-45:49:43.6	-78.2	4.73±0.06	42.9	46.93±0.03
G340.0708+00.9267	16:43:15.69	-44:35:16.0	-73.5	4.69±0.04	93.8	46.96±0.04
G343.5024−00.0145	16:59:20.78	-42:32:37.5	-27.9	2.72±0.08	176.9	47.06±0.12
G345.0034−00.2240A	17:05:11.19	-41:29:06.3	-27.3	2.87±0.08	140.0	46.99±0.12
G345.4881+00.3148	17:04:28.04	-40:46:23.3	-17.9	2.12±0.10	1980.0	47.89±0.21
G346.0774−00.0562	17:07:53.91	-40:31:34.2	-83.9	10.92±0.03	8.3	46.90±0.01
G347.8707+00.0146	17:13:08.77	-39:02:28.2	-30.6	3.42±0.04	206.1	47.33±0.05
G348.8922−00.1787	17:17:00.10	-38:19:26.4	8.13	11.20±0.05	185.7	48.32±0.02

Notes. Columns are (1)source name, (2)right ascension, (3)declination, (4)local standard of rest velocity, (5)distance, (6)flux density at 4.8 GHz $S_{4.8}$, (7)number of UV ionizing photons
a: Urquhart et al. (2007a)

Table 2. Properties of the RMSs.

RMS name	S_{peak}/Ω[a] (Jy/beam)	S_{870}[a] (Jy)	T_d[b] (K)	R_{eff}[a] ($''$)	M_{tot} ($M_\odot$)	N_{H_2}[c] ($\times 10^{22}$ cm^{-2})	$< n_{H_2} >$ ($\times 10^4$ cm^{-3})
G330.2838+00.4933	2.00	7.50	30.0	30	1995±46	2.2	1.5±0.1
G331.4181−00.3546	3.48	39.81	18.9	75	9099±238	6.0	0.3±0.1
G332.2944−00.0962	7.04	34.52	27.6	62	4603±77	8.2	1.3±0.1
G332.5438−00.1277	2.03	26.30	30.5	69	3174±97	2.1	0.6±0.1
G332.8256−00.5498A	32.86	139.92	31.7	79	16246±460	33.5	2.1±0.1
G333.3401−00.1273	1.01	3.43	40.5	28	311±5	0.8	0.9±0.1
G337.0047+00.3226	2.28	6.67	33.9	25	6341±56	2.2	0.8±0.1
G337.4032−00.4037	18.35	58.81	29.0	47	5535±143	20.4	5.4±0.2
G337.7091+00.0932A	9.73	48.94	30.0(A)	66	55045±424	10.5	0.4±0.1
G337.8442−00.3748	3.32	9.90	32.8	31	771±30	3.3	2.9±0.1
G339.1052+00.1490	1.98	8.64	29.6	34	1831±23	2.2	1.4±0.1
G340.0708+00.9267	2.69	15.10	33.4	40	2716±48	2.6	1.3±0.1
G343.5024−00.0145	6.21	45.12	24.8	71	3766±209	8.1	1.6±0.1
G345.0034−00.2240A	18.51	137.14	31.0	113	9850±528	19.3	0.9±0.1
G345.4881+00.3148	17.27	143.50	26.5	77	6782±646	21.0	4.8±0.4
G346.0774−00.0562	2.38	11.57	30.0(A)	43	13013±76	2.6	0.4±0.1
G347.8707+00.0146	3.16	17.56	30.0(A)	45	1922±45	3.4	1.6±0.1
G348.8922−00.1787	3.02	7.80	30.0(A)	17	4177±19	1.8	1.8±0.1

Notes. Columns are (1)source name, (2)peak intensities S_{peak}, (3)flux densities S_{870}, (4)dust temperature, (5)effective radii, (6)clump mass, (7)H_2 column density, (8)volume-averaged H_2 number density
a: Contreras et al. (2013)
b: The T_d values marked with "A" represent the average value derived for other sources.
c: The data has been converted to the Mopra telescope beam size.

velocities of HCO^+ and N_2H^+ should be similar to those of Urquhart et al. (2007b, 2008). (iii)The center locations of RMSs and 870 μm peak emissions are within $18''$, which is about the angular resolution of MSX at 8.0 μm. (iv)Sources should not be on the edge of known HII or supernova regions, considering the large beam of the 22-m Mopra telescope. The information of our selected sources is listed in Table 1. The detection of radio emissions in our sources indicates they are much more evolved, at least be similar to the "active"/"red" stages of IRDCs. However, sources of Hoq et al. (2013) and Miettinen (2014) range from prestellar ("quiescent") to HII regions with bright IR emissions ("red"). We suppose to find different chemical properties of our RMSs using the above archival data.

Table 3. Parameters for molecular lines N_2H^+ and HCO^+.

RMS name	Molecular line	Width (km s^{-1})	T_{ex}[a] (K)	τ	$\int T_{mb}\,dv$ (K km s^{-1})	N ($\times 10^{12}$ cm^{-2})	χ ($\times 10^{-10}$)
G330.2838+00.4933	N_2H^+	2.65± 0.16	11.2 ±0.5	0.14±0.06	3.6± 0.5	5.9±1.7	2.7± 0.8
	HCO^+	3.54± 0.17	12.5±2.5	0.53±0.18	13.3± 1.0	18.3± 1.4	8.3± 0.6
G331.4181−00.3546	N_2H^+	2.34± 0.21	6.2±1.8	1.17± 0.17	10.6± 0.8	13.8±3.2	2.3± 0.5
	HCO^+	4.39± 0.45	12.5±2.5	0.47±0.16	15.5± 2.0	20.9± 2.7	3.5± 0.5
G332.2944−00.0962	N_2H^+	2.88± 0.10	7.2±0.5	0.83±0.12	12.2± 0.4	16.4±2.1	2.0± 0.3
	HCO^+	4.51± 0.40	12.5±2.5	0.23±0.07	9.3± 1.7	11.7± 2.1	1.4± 0.2
G332.5438−00.1277	N_2H^+	1.90± 0.18	7.8±1.4	0.41± 0.27	4.5± 0.3	6.3± 0.3	3.0± 0.3
	HCO^+	2.70± 0.14	12.5±2.5	0.64±0.23	4.1± 0.2	5.8± 0.3	2.8± 0.1
G332.8256−00.5498A	N_2H^+	4.19± 0.21	8.9±2.3(A)	...	16.2± 2.4	23.6± 3.9	0.8± 0.1
	HCO^+	11.84± 0.31	12.5±2.5	0.49±0.16	31.0± 0.3	42.2± 0.4	1.3± 0.1
G333.3401−00.1273	N_2H^+	2.10± 0.29	8.9±2.3(A)	...	2.8± 0.4	4.0±1.2	5.0± 1.5
	HCO^+	2.47± 0.26	12.5±2.5	0.20±0.06	4.1± 1.2	5.1± 1.5	6.4± 1.8
G337.0047+00.3226	N_2H^+	3.76± 0.21	8.9±2.3(A)	...	2.9± 0.5	4.1± 1.0	1.5±0.5
	HCO^+	4.63± 0.25	12.5±2.5	0.40±0.13	13.9± 1.6	18.4± 2.1	8.4± 1.0
G337.4032−00.4037	N_2H^+	3.16± 0.01	10.4±1.3	0.47±0.05	13.2± 0.4	20.7±1.2	1.0± 0.1
	HCO^+	6.49± 0.18	12.5±2.5	0.51±0.17	20.9± 1.5	28.6± 2.1	1.4± 0.1
G337.7091+00.0932A	N_2H^+	4.02± 0.29	7.5±0.6	0.40± 0.27	8.9± 0.7	12.3± 2.2	1.2± 0.2
	HCO^+	5.40± 0.31	12.5±2.5	0.35±0.11	15.1± 0.7	19.7± 0.9	1.9± 0.1
G337.8442−00.3748	N_2H^+	2.36± 0.12	8.9±2.3(A)	...	6.2± 0.2	9.1±1.2	2.8± 0.4
	HCO^+	2.41± 0.26	12.5±2.5	0.25±0.08	4.9± 0.2	6.2± 0.3	1.9± 0.1
G339.1052+00.1490	N_2H^+	2.62± 0.16	12.1±0.5	0.2±0.07	6.5± 0.4	11.1±2.8	5.0±0.3
	HCO^+	4.01± 0.42	12.5±2.5	0.21±0.06	7.4± 2.2	9.2± 2.7	4.2± 1.2
G340.0708+00.9267	N_2H^+	3.58± 0.19	4.1±0.5	2.1±0.35	7.5± 1.0	10.0±1.2	3.8± 0.5
	HCO^+	3.41± 0.11	12.5±2.5	0.93±0.38	17.9± 0.9	27.0± 1.4	10.4± 0.5
G343.5024−00.0145	N_2H^+	3.13± 0.10	9.9±0.5	0.76±0.01	17.1± 0.6	26.2±2.5	3.2± 0.3
	HCO^+	3.75± 0.23	12.5±2.5	0.55±0.19	15.0± 1.0	20.7± 1.4	2.6± 0.2
G345.0034−00.2240A	N_2H^+	4.21± 0.16	4.4±0.5	2.0±0.30	12.8± 0.8	16.7±1.7	0.9± 0.1
	HCO^+	5.02± 0.39	12.5±2.5	0.20±0.04	9.6± 0.4	12.1± 0.5	0.6± 0.1
G345.4881+00.3148	N_2H^+	3.83± 0.13	5.6±0.5	1.7±0.10	17.5± 1.5	22.6±3.3	1.1± 0.2
	HCO^+	5.21± 0.19	12.5±2.5	1.29±0.20	43.2± 2.8	96.4± 6.2	4.6± 0.3
G346.0774−00.0562	N_2H^+	3.12± 0.24	9.5±0.5	0.46± 0.19	10.6± 0.6	16.0± 0.7	6.1± 0.3
	HCO^+	2.59± 0.24	12.5±2.5	0.32±0.10	6.2± 1.1	8.0± 1.4	3.1± 0.6
G347.8707+00.0146	N_2H^+	4.40± 0.29	8.9±2.3(A)	...	8.0± 0.5	11.6±1.1	3.4 ± 0.3
	HCO^+	9.02± 0.31	12.5±2.5	0.35±0.11	17.5± 1.0	22.8± 2.0	6.7± 0.6
G348.8922−00.1787	N_2H^+	3.23± 0.23	8.9±2.3(A)	...	3.1± 0.5	4.4±1.6	1.3± 0.3
	HCO^+	5.70± 0.20	12.5±2.5	0.50±0.17	20.2± 1.4	27.5± 1.9	8.3± 0.6

Notes. Columns are (1)source name, (2)Molecular line name, (3)Line width, (4)excitation temperature, (5)optical depth, (6)integrated intensity, (7)total column density, (8)fractional abundance with respect to H_2.
a: The T_{ex} of N_2H^+ values marked with "A" represent the average value derived for other sources.

3 RESULTS AND ANALYSIS

3.1 Physical parameters

The dust temperature (T_d) is essential to study the physics and chemistry of star formation. For those sources in our sample that are associated with IRAS point sources, we estimated the dust temperature to be the same as the 60/100 μm color temperature defined by Henning et al. (1990) as

$$T_d \simeq T_c(\frac{60}{100}) = 96[(3+\beta)ln(\frac{100}{60}) - ln(\frac{S_{60}}{S_{100}})]^{-1} \quad (2)$$

where β is the dust emissivity index set to be 1.8 to be consistent with the Ossenkopf & Henning (1994) dust model. S_λ is the flux density at the wavelength λ. The derived values are listed in Table 2. The mean dust temperature is about 30 K, which is much larger than those in IRDCs (e.g. Miettinen & Harju 2010; Hoq et al. 2013), indicating our sources are more evolved. Four of our sources are not associated with any IRAS point source. For these sources we assume their dust temperature to be 30 K. Masses will be underestimated if the temperature is lower than the assumed value of 30 K. For example, at 20 K the masses will be higher by a factor of 1.7.

Assuming that the dust emission at 870 μm is optically thin, the clump masses and H_2 column densities could be estimated through the following expressions:

$$M_{tot} = \frac{S_{870}D^2R}{B_{870}(T_d)\kappa_{870}} \quad (3)$$

$$N_{H_2} = \frac{S_{peak}R}{\Omega B_{870}(T_d)\kappa_{870}m_{H_2}} \quad (4)$$

where S_{870} is the integrated flux density. S_{peak} denotes the peak flux density. D is the distance to the RMS. Ω is the beam solid angle. R is the gas-to-dust mass ratio which is set to be 100. m_{H_2} is the mass of one hydrogen molecule. $B_{870}(T_d)$ is the Planck function at the dust temperature T_d. We assumed that $\kappa_{870} = 0.17$ m^2 kg^{-1} (Miettinen & Harju 2010). The derived masses are inverse proportional to the

assumed value of the opacity κ_{870}, which has an uncertainty of at least a factor 1.5.

The volume-averaged H_2 number densities ($< n(H_2) >$) could be calculated assuming a spherical geometry for the clumps, using these formula

$$< \rho >= \frac{3M_{tot}}{4\pi R_{eff}^3} \quad (5)$$

$$< n(H_2) >= \frac{< \rho >}{\mu_{H_2} m_H} \quad (6)$$

The linear clump effective radii is derived from the angular radii and kinematic distances as R_{eff} (pc) = R_{eff}(rad) × D(pc). The value of R_{eff}(rad) is from Contreras et al. (2013). We adopt a mean molecular weight per H_2 molecule of $\mu = 2.8$ to include helium. The derived parameters are listed in Table 2. Taking into account the spatial resolution effects, the derived column densities are all beyond the column density threshold required by theoretical considerations for massive star formation.

3.2 Chemical parameters

Figures 3-20 show the N_2H^+ (1-0) and HCO^+ (1-0) spectra on the peak emissions of 870 μm and their integrated intensities superimposed on the 870 μm images of the RMSs. Most of the detected N_2H^+ and HCO^+ emissions match well with the dust emission, implying a close link to their chemical evolution in the RMSs. The HCO^+ emission lines of some sources are far of having a simple Gaussian shape, presenting asymmetries, and spectral wings or shoulders, which suggest that the molecular gas is affected by the dynamics of these star-forming regions. Yu & Wang (2014) made a study of 19 RMSs and find these profiles are probably caused by infall and/or outflow activities. Some of our sources are also included in their study. The N_2H^+ (1-0) line has 15 hyperfine structures (HFS) out of which seven have a different frequency (e.g. Pagani et al. 2009; Keto & Rybicki 2010). These velocity components blend into three groups (see figure 2 of Purcell et al. 2009). We followed the procedure outlined by Purcell et al. (2009) to estimate the optical depth of N_2H^+. Assuming the line widths of the individual hyperfine components are all equal, the integrated intensities of the three blended groups should be in the ratio of 1:5:3 under optically thin conditions. The optical depth can then be derived from the ratio of the integrated intensities ($\int T_{MB} dv$) of any groups using the following equation:

$$\frac{\int T_{MB,1} dv}{\int T_{MB,2} dv} = \frac{1 - exp(-\tau_1)}{1 - exp(-a\tau_2)} \quad (7)$$

where a is the expected ratio of τ_2/τ_1 under optically thin conditions. We determined the optical depth only from the intensity ratio of group 1/group 2, as anomalous excitation of the F_1F = 10-11 and 12-12 components (in our group 3) has been reported by Caselli et al. (1995). The optical depth of group 2 is listed in table 3 because it provides a better estimate for the excitation temperature when $\tau > 0.1$. Then the excitation temperature (T_{ex}) for N_2H^+ could be calculated with the following formula:

$$T_{ex} = 4.47/ln(1 + (\frac{T_{MB}}{4.47(1 - exp(-\tau))} + 0.236)^{-1}) \quad (8)$$

The N_2H^+ optical depth of our six clumps could not be derived through this method. For these cases, we adopted the mean derived excitation temperature. Assuming local thermodynamic equilibrium (LTE) and using Eq. (2) in Miettinen (2014), we derived the column densities of N_2H^+. Finally, the fractional abundance of N_2H^+ with respect to H_2 could be estimated by χ (N_2H^+) = N(N_2H^+)/N(H_2). The derived parameters are listed in Table 3.

Generally speaking, the optical depth and T_{ex} of HCO^+ could be derived by comparing the intensities of HCO^+ and $H^{13}CO^+$. However, the $H^{13}CO^+$ emission was not detected in most cases. For the sources (G332.8256-00.5498A, G337.4032-00.4037, G345.0034-00.2240A and G345.4881+00.3148) which show distinct $H^{13}CO^+$ emissions, we derive the optical depths of HCO^+ from

$$\frac{^{12}T_{mb}}{^{13}T_{mb}} = \frac{1 - exp(-\tau_{12})}{1 - exp(-\tau_{12}/X)} \quad (9)$$

where τ_{12} is the optical depth of the HCO^+ gas and X is the isotope abundance ratio

$$X = \frac{N_{HCO^+}}{N_{H^{13}CO^+}} = \frac{\chi(HCO^+)}{\chi(H^{13}CO^+)} \simeq \frac{[^{12}C]}{[^{13}C]} \quad (10)$$

The Galactic gradient in the $^{12}C/^{13}C$ ratio ranges from ∼20 to ∼70 (see Savage et al. 2002, and references therein). And the ratio of $\frac{\chi(HCO^+)}{\chi(H^{13}CO^+)}$ may also be affected by chemistry. Thus, we assumed a constant $X = 50$. We then can calculate the excitation temperature according to

$$T_{ex} = 4.28(ln(1 + 4.28[\frac{T_{mb}}{f(1 - exp(-\tau_\nu))} + J(T_{bg})]^{-1}))^{-1} \quad (11)$$

where f is the filling factor, here we assume it to be 1. The derived excitation temperature is 6.3K, 6.4K, 4.7K and 12.3K respectively. Our values are considerably lower than the $\sim 10 - 15$K temperature in previous work (e.g. Girart et al. 2000). Purcell et al. (2006) regard that the emission is beam diluted in a significant fraction. If the emission is smaller than the beam, the filling factor f will be less than 1 and the excitation temperature will be underestimated. In our final analysis, we have assumed an excitation temperature of 10 − 15 K and the column densities are calculated by Eq. (4) in Liu et al. (2013). The fractional abundance of HCO^+ with respect to H_2 could be estimated by χ (HCO^+) = N(HCO^+)/N(H_2). The derived parameters are also listed in Table 3. From Table 3 we find the optical depths of HCO^+ are less than 1. Considering the fact that HCO^+ emission should be optically thick, the optical depths in our results are probably underestimated.

4 DISCUSSIONS

4.1 Ionized accretion?

The HCO^+ (1-0) lines show non-gaussian profiles in our four sources (G332.8256-00.5498A, G337.4032-00.4037, G345.0034-00.2240A, and G345.4881+00.3148).By position-velocity (PV) diagram and the method described by Mardones et al. (1997), Yu & Wang (2014) found recent outflow activities in G332.8256-00.5498A, G345.0034-00.2240A and G345.4881+00.3148. Large scale infall has also been discovered in G345.0034-00.2240A and G345.4881+00.3148.

From the 4.8 GHz radio observations of ATCA, we can see HCHII/UCHII regions have already formed inside. The sound speed in $\sim 10^4$ K photo-ionized gas is about 10 km s^{-1}, larger than the escape speeds in galactic molecular cores (see Fig. 1 in Tan et al. 2014). This means if the gas in a massive star formation region gets ionized, the gas pressure will drive a thermal pressure that may chock off accretion. It is still unclear whether accretion can continue in some form such as through an ionized accretion flow. The high resolution observations of H66α taken at the VLA have directly shown an ionized accretion in G10.62-0.38 (Keto & Wood 2006), while accretion in G5.89-0.39 seems to have halted at the onset of the UCHII region (Klassen et al. 2006). We here discuss whether (ionized) accretion could continue in G345.4881+00.3148.

We can determine the infall velocity using the two layer radiative transfer model of Myers et al. (1996). Using their equation (9):

$$V_{in} \approx \frac{\sigma^2}{v_{red} - v_{blue}} ln(\frac{1 + eT_{BD}/T_D}{1 + eT_{RD}/T_D}) \quad (12)$$

where T_D, T_{BD} and T_{RD} are the brightness temperature of the dip, the height of the blue peak above the dip and the height of the red peak above the dip respectively. The velocity dispersion σ can be obtained from the FWHM of $H^{13}CO^+$ (1-0). The gaussian-fitted lines of HCO^+ and $H^{13}CO^+$ is shown in figure 17. We find G345.4881+00.3148 has an infall velocity of about 4.2 km s^{-1} in large scale. To estimate the mass infall rate, we use Eq. (3) of Klassen & Wilson (2007) $dM/dt = (4/3)\pi < n_{H_2} > \mu\ m_H\ r^2\ V_{in}$, where μ means molecular weight, m_H is the mass of Hydrogen, r is the radius of the emitting region (here is set to be the beam radius), V_{in} is the infall velocity, and $< n_{H_2} >$ is the ambient density calculated above. From the analysis above, we estimate mass infall rate of G345.4881+00.3148 is about 2.1×10^{-3} $M_\odot$ yr^{-1}. This value is much higher than those generally observed in low-mass star forming regions.

Walmsley (1995) considered the accretion flow in free-fall onto a star, and showed that the escape speed from the edge of the ionized region will exceed the ionized gas sound speed c_i if the accretion rate satisfies

$$\frac{dM}{dt} > [\frac{8\pi m_H^2 GMS}{2.2\alpha_B ln(v_{esc}/c_i)}] = 4 \times 10^{-5} (\frac{M}{100 M_\odot} \frac{N_L}{10^{49} s^{-1}})^{1/2} M_\odot yr^{-1} \quad (13)$$

where M is the central stellar mass, m_H is the mean mass per H nucleus, α_B is the case B recombination coefficient and v_{esc} is the escape speed from the stellar surface. The numerical evaluation uses $v_{esc} = 1000$ km s^{-1} and $c_i = 10$ km s^{-1} (The result is unsensitive to these parameters). Our calculated mass infall rate is sufficient to allow continuing accretion onto an B0 (G345.4881+00.3148) type star. Like the case of G10.6-0.4, accretion flow in this region may be ionized. However, given the low angular resolution of the data (at 2.1 kpc, 38″ is over half a parsec), it is also possible that a lower mass star is forming in the vicinity. High angular resolution observations are needed to verify our speculations.

4.2 N_2H^+ and HCO^+

N_2H^+ is widely detected in low- and high-mass prestellar and protostellar cores, owing to its resistance of depletion at low temperature and high densities. We find that its line widths for our RMSs vary in the range from 1.9 to 4.4 km s^{-1}, much larger than those found in low-mass prestellar cores (Lee et al. 2001). This large line width can not be purely explained by thermal motions. Internal turbulence may dominate in massive star formation regions (Myers & Fuller 1992; Caselli & Myers 1995). Chambers et al. (2006) and Vasyunina et al. (2011) found that the line widths and the integrated intensities of N_2H^+ have a trend to larger values, from "quiescent", "middle(or intermediate)" to "active" clumps in IRDCs. They regarded it was because that "active" sources are more evolved and present further evolutionary stages compared with "quiescent" sources. The mean line width of our RMSs is 3.2 km s^{-1}, larger than the mean value of their "active" clumps. It is probably that our sources are much more evolved. However, our mean integrated intensity of N_2H^+ is only 10 K km s^{-1}, between their "middle" and "active" clump values. In our sources, we found N_2H^+ column densities in the range of $4.0 \times 10^{12} - 2.6 \times 10^{13}$ cm^{-2}, and abundances of $0.9 \times 10^{-10} - 6.1 \times 10^{-10}$. The average values are 1.6×10^{13} cm^{-2} and 3.0×10^{-10}, respectively. Vasyunina et al. (2011) derived fractional N_2H^+ abundances of $1.9 \times 10^{-10} - 8.5 \times 10^{-9}$ with an average of 2.8×10^{-9} for their IRDCs. Miettien (2014) derived similar fractional N_2H^+ abundances of $2.8 \times 10^{-10} - 9.8 \times 10^{-9}$ with an average of 1.6×10^{-9}. Our value of χ (N_2H^+) is nearly one order less than these observations. Chemical models indicate when dust temperature exceeds 20 K, CO would be evaporated from the dust grains. The enhanced CO abundance will destroy N_2H^+ producing HCO^+. The mean dust temperature of our sources is about 30 K, much larger than that in IRDCs ($\sim$ 15 K). Previous molecular-line observations have also shown the typical gas kinetic temperature of IRDCs clumps lies in the range of 10 and 20 K (e.g. Sridharan et al. 2005; Sakai et al. 2008; Ragan et al. 2011). This may be the reason why our values of χ (N_2H^+) are much smaller.

HCO^+ can be formed through $N_2H^+ + CO \rightarrow HCO^+ + N_2$ when CO is evaporated from the dust grains. The HCO^+ abundance can also be increased in regions where shocks are generated (e.g. the gas through which a protostellar outflow is passing). Our HCO^+ column densities range from 5.1×10^{12} cm^{-2} to 9.6×10^{13} cm^{-2} (2.4×10^{13} cm^{-2} on average). These values are very close to those of Miettien (2014), and are higher by a factor of about five on average than those derived by Liu et al. (2013). As shown in figure 1, there is a hint that the fractional abundance of HCO^+ increases as a function of the N_2H^+ abundance. A least squares fit to the data points yields $\log[\chi\ (HCO^+)] = (0.76\pm0.51) + (1.07\pm0.05)\log[\chi\ (N_2H^+)]$, with the linear Pearson correlation coefficient of $r = 0.61$. The trend is consistent with theoretical models. Because CO is both the main supplier of HCO^+ and the main destroyer of N_2H^+, this suggests that the HCO^+ abundance increases with respect to N_2H^+ as sources evolve to a warmer phase. N_2H^+ can also be destroyed in the electron recombination: $N_2H^+ + e^- \rightarrow N_2 + H$ or $NH + N$ (e.g. Dislaire et al. 2012; Vigren et al. 2012). We tried to find a relationship between the N_2H^+

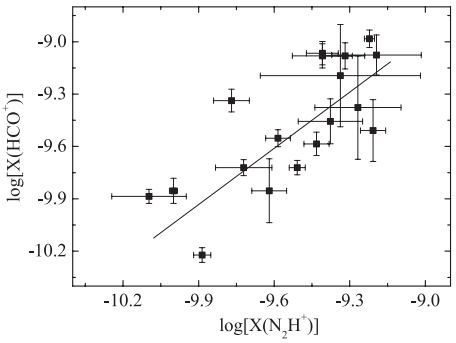

Figure 1. HCO^+ fractional abundances vs. N_2H^+ fractional abundances.

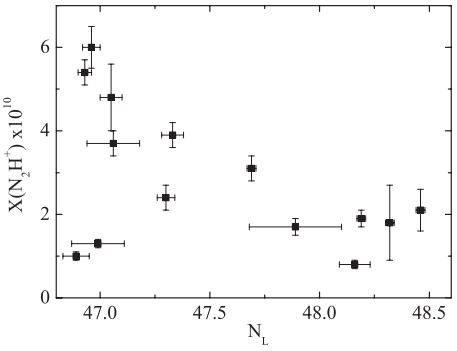

Figure 2. N_2H^+ fractional abundance plotted as a function of N_L in logarithmic scales.

fractional abundance and Lyman continuum fluxes (N_L). Figure 2 seems to show that $\chi(N_2H^+)$ decreases as a function of N_L. UV radiation field may have an influence on the chemistry of N_2H^+ in the RMSs. Since our limited data, more studies should be done in the near future to check out this conclusion.

5 SUMMARY

Using archival data taken from ATLASGAL, ATCA, and MALT90, we have studied the physical and chemical properties of 18 southern RMSs (HII regions), and compared our results with previous observations of IRDCs. Our sources are much more evolved than general IRDCs. The H_2 column densities and gas number densities have been derived. Ionized accretion may be taking place in G345.4881+00.3148. Most of the detected N_2H^+ and HCO^+ emissions match well with the dust emission, implying a close link to their chemical evolution in the RMSs. We found the abundance of N_2H^+ is one order of magnitude lower than in other surveys of IRDCs, and a positive correlation between the abundances of N_2H^+ and HCO^+. The fractional abundance of N_2H^+ with respect to H_2 decreases as a function of N_L. It seems that the UV radiation field has an influence on the chemistry of N_2H^+ in the RMSs. Like the chemical model of low-mass star formation theory, these observed trends could be interpreted as an indication of enhanced destruction of N_2H^+, either by CO or through dissociative recombination with electrons produced by central UV photons.

ACKNOWLEDGEMENTS

We thank the anonymous referee for his constructive suggestions. This paper made use of information from the Red MSX Source (RMS) survey database http://rms.leeds.ac.uk/cgi-bin/public/RMS_DATABASE.cgi which was constructed with support from the Science and Technology Facilities Council of the UK. This research made use of data products from the Millimetre Astronomy Legacy Team 90 GHz (MALT90) survey. The Mopra telescope is part of the Australia Telescope and is funded by the Commonwealth of Australia for operation as National Facility managed by CSIRO.

REFERENCES

Bergin, E. A., & Tafalla, M. 2007, ARA&A, 45, 339
Caselli, P., & Myers, P. C., 1995 ApJ, 446, 665.
Caselli, P., Myers, P. C., Thaddeus, P., 1995, ApJ, 455, 77
Chambers, E. T., Jackson, J. M., Rathborne, J. M., & Simon, R. 2009, ApJS, 181, 360
Chaisson, E. J. 1976, in Fronters of Astrophysi cs, 259
Contreras, Y., Schuller, F., Urquhart, J.S., et al. 2013, A&A, 549, A45
Dislaire, V., Hily-Blant, P., Faure, A., Maret, S. et al. 2012, A&A, 537, 20A
Foster, J. B., Jackson, J. M., Barris, E. et al., 2011, ApJS, 197, 25
Girart, J. M., Estalella, R., Ho, P. T. P., Rudolph, A. L., 2000, ApJ, 539, 763
Henning, T., Pfau, W., & Altenhoff, W. J. 1990, A&A, 227, 542
Herbst, E., & Klemperer, W., 1973, ApJ, 185, 505
Hirota, T., Yamamoto, S., Mikami, H., & Ohishi, M. 1998, ApJ, 503, 717
Hoq, S., Jackson, J. M., Foster, J. B., et al. 2013, ApJ, 777, 157
Keto, E., & Rybicki, G., 2010, ApJ, 716, 1315
Keto, E., Wood, K., 2006, ApJ, 637, 850
Klassen, P.D., Plume, R., Ouyed, R., von BendaBeckmann, A. M, Di Francesco, J., 2006, ApJ, 648, 1079
Klaassen, P.D., Wilson, C.D., 2007, ApJ, 663, 1092
Kurtz, S., Cesaroni, R., Churchwell, E., Hofner, P., & Walmsley, C. M. 2000, in Protostars and Planets IV, eds. V. Mannings, A. P. Boss, & S. S. Russell (Tucson: Univ. of Arizona Press), 299
Ladd, N., Purcell, C.,Wong, T., Robertson, S., 2005, Publ. Astron. Soc. Aust., 22, 62
Lee, C. W., Myers, P. C., & Tafalla, M. 2001, ApJS, 136, 703
Lee, J.-E., Bergin, E. A., & Evans, N. J., II, 2004, ApJ, 617, 360
Lee, J.-E., Evans, N. J., II, Shirley, Y. L., & Tatematsu, K., 2003, ApJ, 583, 789
Liu, X.-L.,Wang, J.-J., & Xu, J.-L. 2013, MNRAS, 431, 27
Lumsden S. L., Hoare M. G., Urquhart, J. S. et al. 2013, ApJS, 208, 11
Lumsden, S. L., HoareM. G., Oudmaijer, R. D., Richards, D., 2002, MNRAS, 336, 621

Mardones, D., Myers, P. C., Tafalla, M., Wilner, D. J., Bachiller, R., Garay, G., 1997, ApJ, 489, 719
Myers, P. C., & Fuller, G. A., 1992 ApJ, 396, 631.
Myers, P.C., Mardones, D., Tafalla, M., Williams, J.P., Wilner, D.J., 1996, ApJ, 465, L133
Miettinen, O., & Harju, J., 2010, A&A, 520, A102
Miettinen, O., 2014, A&A, 562, A3
Ossenkopf, V., & Henning, T. 1994, A&A, 291, 943
Pagani, L., Daniel, F., & Dubernet, M.-L. 2009, A&A, 494, 719
Purcell, C. R., Balasubramanyam, R., Burton, M. G., et al. 2006, MNRAS, 367, 553
Purcell, C. R., Longmore, S. N., Burton, M. G., et al. 2009, MNRAS, 394, 323
Ragan, S. E., Bergin, E. A., & Wilner, D. 2011, ApJ, 736, 163
Sakai, T., Sakai, N., Kamegai, K., et al. 2008, ApJ, 678, 1049
Sanhueza, P., Jackson, J. M., Foster, J. B., et al. 2012, ApJ, 756, 60
Savage, C., Apponi, A. J., Ziurys, L. M., Wyckoff, S., 2002, ApJ, 578, 211
Snyder, L. E., Hollis, J. M., & Watson, W. D. 1977, ApJ, 212, 79
Sridharan, T. K., Beuther, H., Saito, M., et al. 2005, ApJ, 634, L57
Siringo, G., Kreysa, E., et al. 2009, A&A, 497, 945
Tan, J. C., Beltran, M. T., Caselli, P., et al. 2014, in Protostars and Planets VI, ed. H. Beuther et al., in press (arXiv:1402.0919)
Tobin, J. J., Bergin, E. A., Hartmann, L., et al. 2013, ApJ, 765, 18
Turner, B. E., & Thaddeus, P. 1977, ApJ, 211, 755
Urquhart, J. S., Busfield, A. L., Hoare, M. G., et al. 2007a, A&A, 461, 11
Urquhart, J. S., Busfield, A. L., Hoare, M. G., et al. 2007b, A&A, 474, 891
Urquhart, J. S., Busfield, A. L., Hoare, M. G., et al. 2008, A&A, 487, 253
Vasyunina, T., Linz, H., Henning, Th., Stecklum, B., et al. 2009, A&A, 499, 149
Vasyunina, T., Linz, H., Henning, Th., Zinchenko, I., Beuther, H., Voronkov, M., 2011, A&A, 527, A88
Vigren, E., Zhaunerchyk, V., Hamberg, M., Kaminska, M., Semaniak, J. et al. 2012, ApJ, 757, 34
Walmsley, M. 1995, in Revista Mexicana de Astronomia y Astrofisica Conference Series, 137
Yu, N. P., Wang, J. J., 2014, MNRAS, 440, 1213
Zinnecker, H., & Yorke, H. W., 2007, ARA&A, 45, 481

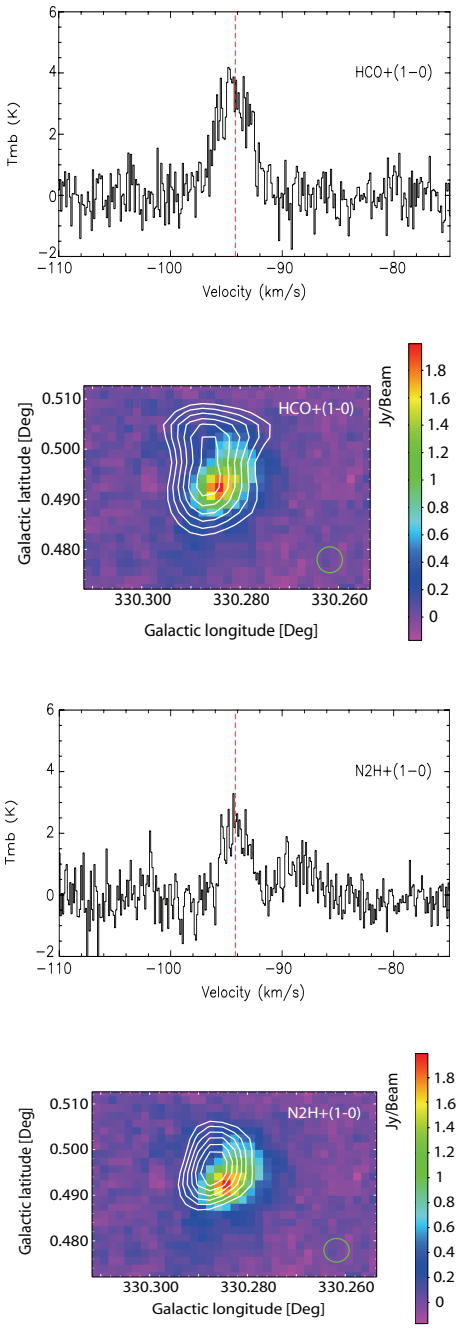

Figure 3. Spectra and integrated intensities superimposed on the 870 μm map in gray scale of G330.2838+00.4933. The red dash line represents the V_{LSR} of N_2H^+ line. Contour levels are 30%, 40%...90% of the center peak emissions. The angular resolution of the ATLASGAL survey is indicated by the green circle shown in the lower right corner.

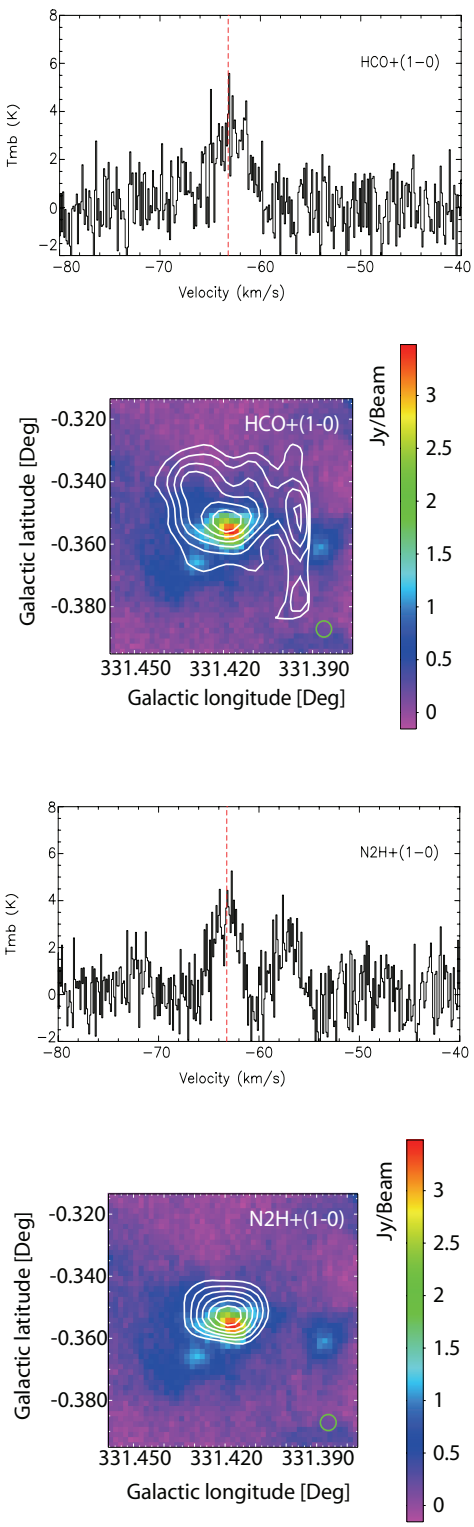

Figure 4. Spectra and integrated intensities superimposed on the 870 μm map in gray scale of G331.4181-00.3546. The red dash line represents the V_{LSR} of N_2H^+ line. Contour levels are 30%, 40%...90% of the center peak emissions. The angular resolution of the ATLASGAL survey is indicated by the green circle shown in the lower right corner.

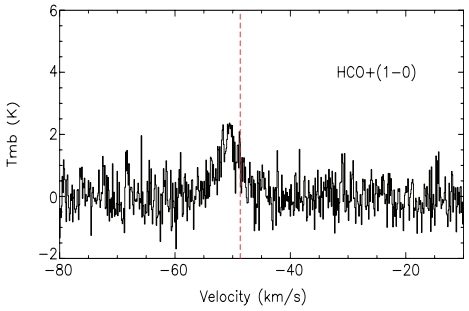

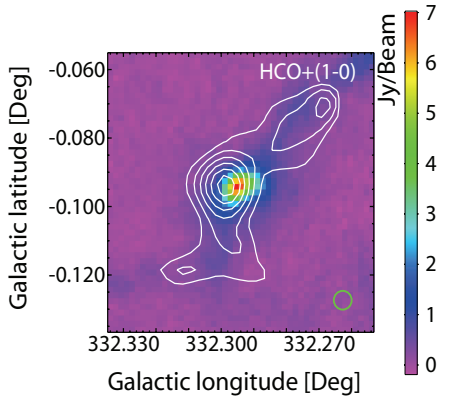

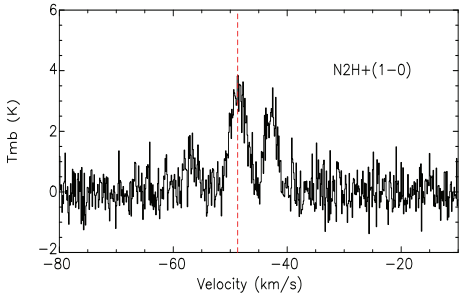

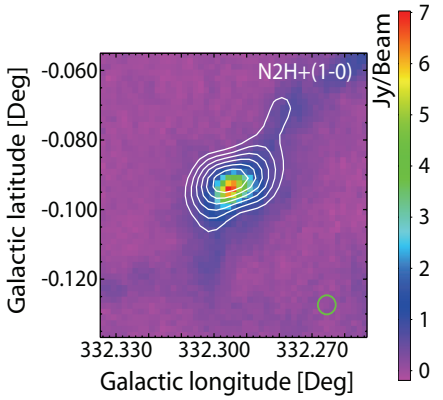

Figure 5. Spectra and integrated intensities superimposed on the 870 μm map in gray scale of G332.2944-00.0962. The red dash line represents the V_{LSR} of N_2H^+ line. Contour levels are 30%, 40%...90% of the center peak emissions. The angular resolution of the ATLASGAL survey is indicated by the green circle shown in the lower right corner.

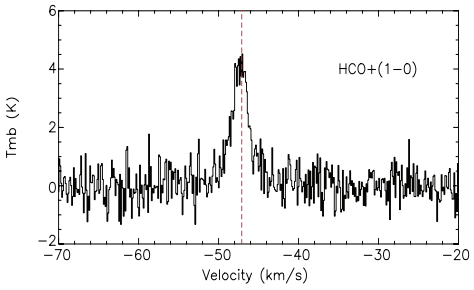

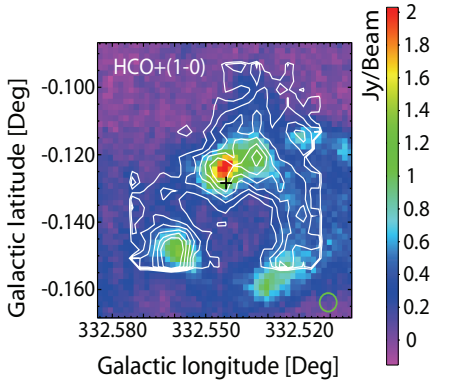

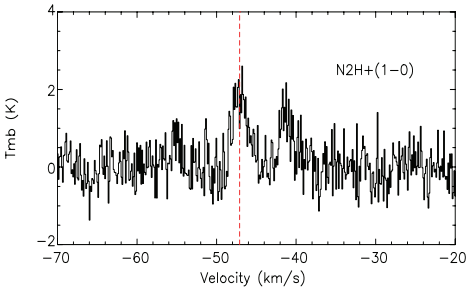

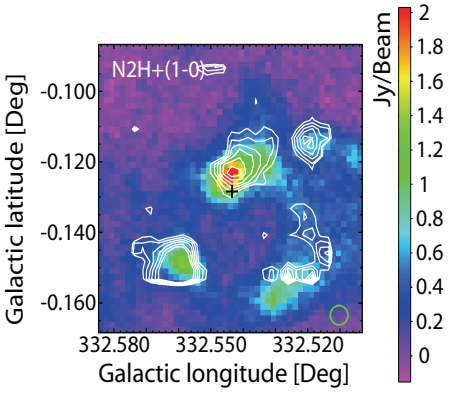

Figure 6. Spectra and integrated intensities superimposed on the 870 μm map in gray scale of G332.5438-00.1277. The red dash line represents the V_{LSR} of N_2H^+ line. Contour levels are 30%, 40%...90% of the center peak emissions. The black cross marks the location of G332.5438-00.1277. The angular resolution of the ATLASGAL survey is indicated by the green circle shown in the lower right corner.

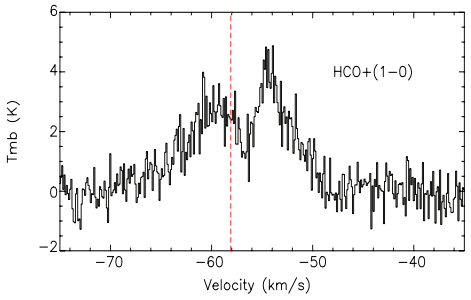

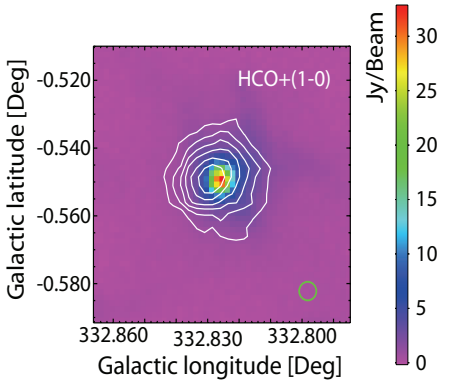

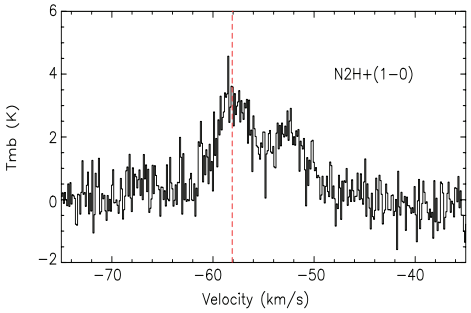

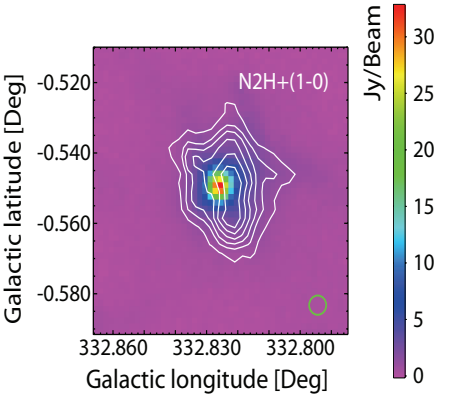

Figure 7. Spectra and integrated intensities superimposed on the 870 μm map in gray scale of G332.8256-00.5498A. The red dash line represents the V_{LSR} of N_2H^+ line. Contour levels are 30%, 40%...90% of the center peak emissions. The angular resolution of the ATLASGAL survey is indicated by the green circle shown in the lower right corner.

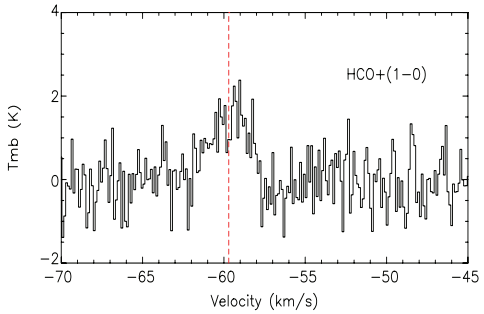

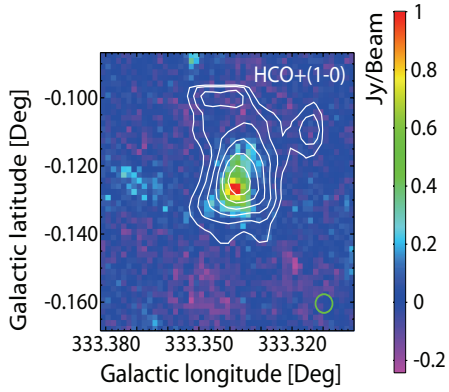

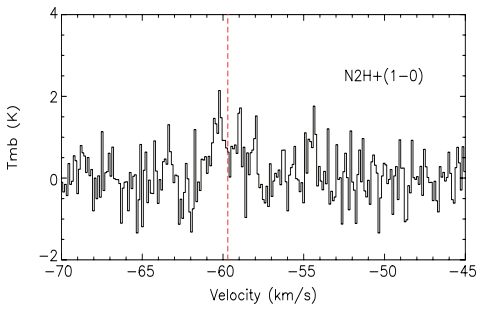

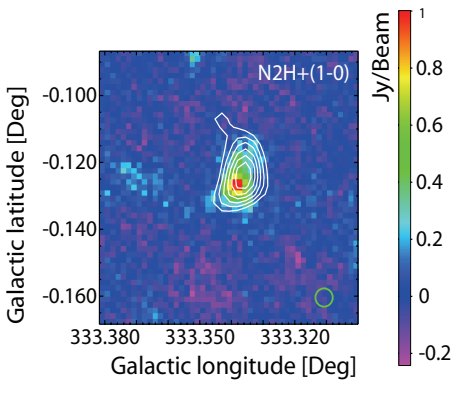

Figure 8. Spectra and integrated intensities superimposed on the 870 μm map in gray scale of G333.3401-00.1273. The red dash line represents the V_{LSR} of N_2H^+ line. Contour levels are 30%, 40%...90% of the center peak emissions. The angular resolution of the ATLASGAL survey is indicated by the green circle shown in the lower right corner.

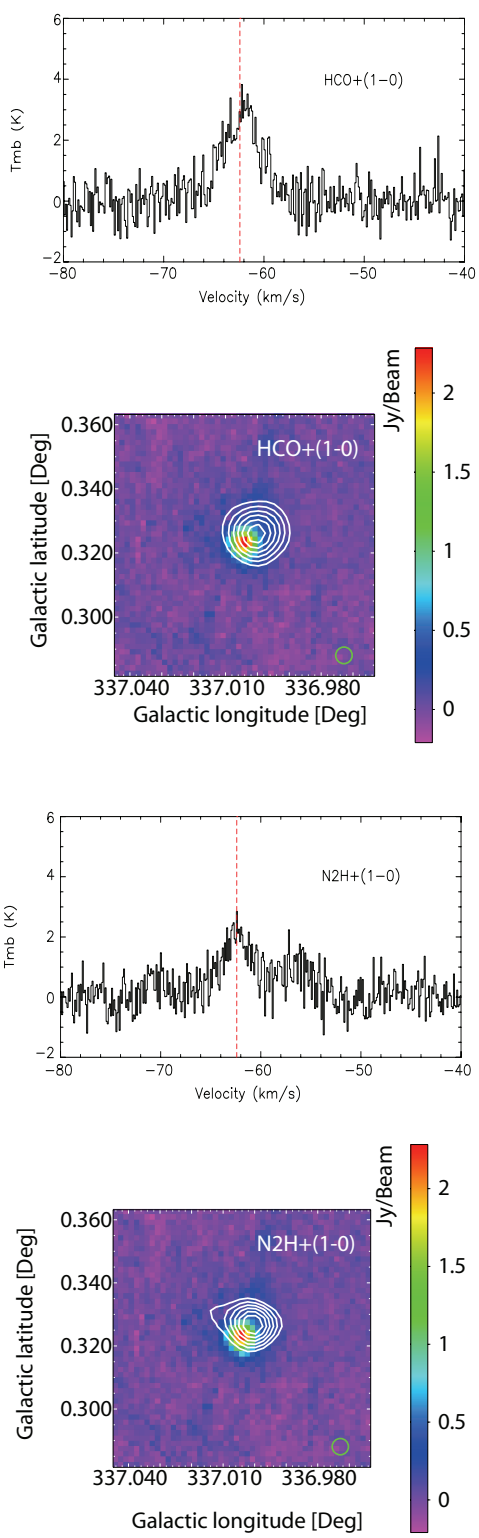

Figure 9. Spectra and integrated intensities superimposed on the 870 μm map in gray scale of G337.0047+00.3226. The red dash line represents the V_{LSR} of N_2H^+ line. Contour levels are 30%, 40%...90% of the center peak emissions. The angular resolution of the ATLASGAL survey is indicated by the green circle shown in the lower right corner.

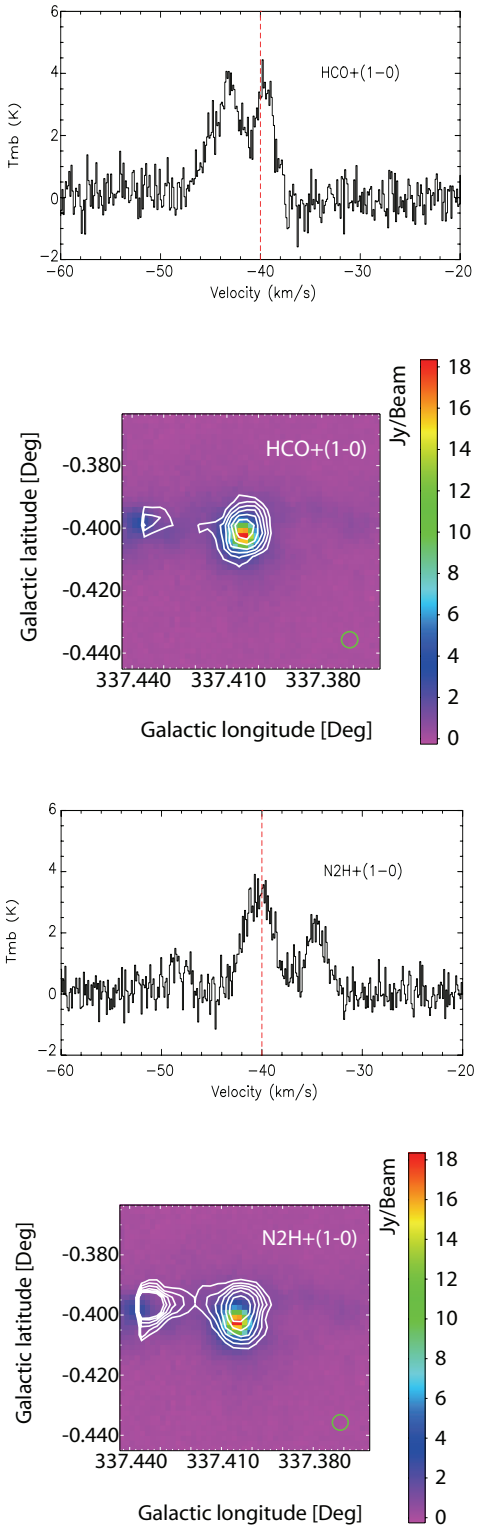

Figure 10. Spectra and integrated intensities superimposed on the 870 μm map in gray scale of G337.4032-00.4037. The red dash line represents the V_{LSR} of N_2H^+ line. Contour levels are 30%, 40%...90% of the center peak emissions. The angular resolution of the ATLASGAL survey is indicated by the green circle shown in the lower right corner.

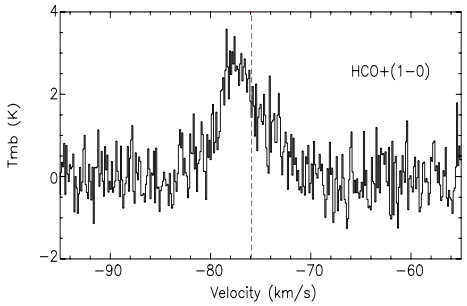

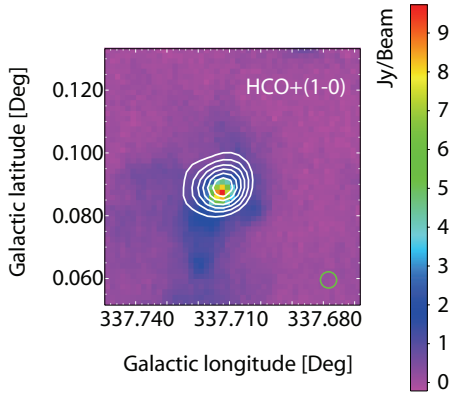

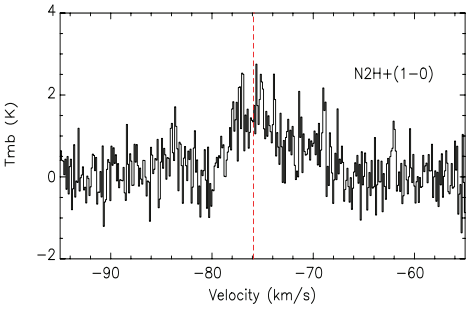

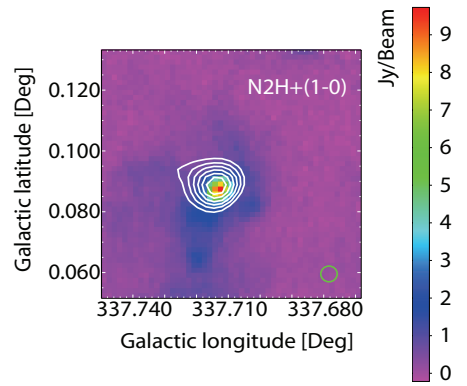

Figure 11. Spectra and integrated intensities superimposed on the 870 μm map in gray scale of G337.7091+00.0932A. The red dash line represents the V_{LSR} of N_2H^+ line. Contour levels are 30%, 40%...90% of the center peak emissions. The angular resolution of the ATLASGAL survey is indicated by the green circle shown in the lower right corner.

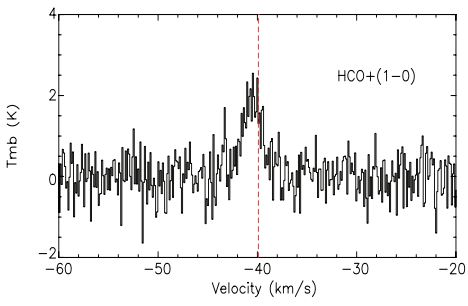

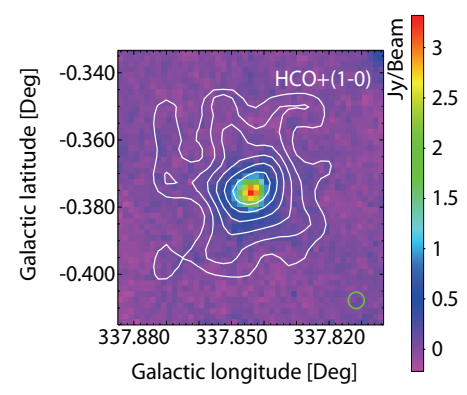

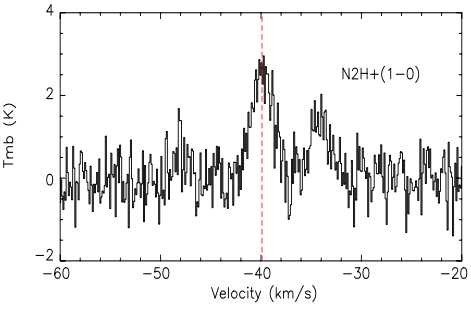

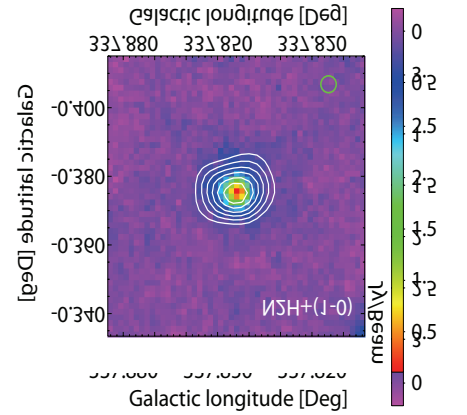

Figure 12. Spectra and integrated intensities superimposed on the 870 μm map in gray scale of G337.8442-00.3748. The red dash line represents the V_{LSR} of N_2H^+ line. Contour levels are 30%, 40%...90% of the center peak emissions. The angular resolution of the ATLASGAL survey is indicated by the green circle shown in the lower right corner.

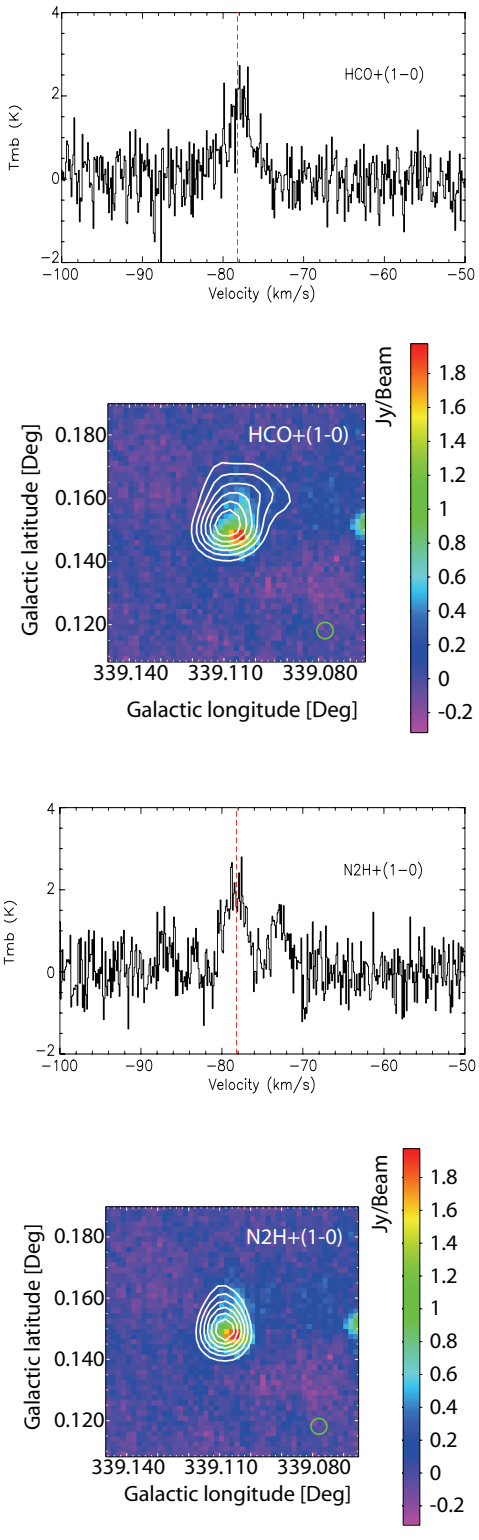

Figure 13. Spectra and integrated intensities superimposed on the 870 μm map in gray scale of G339.1052+00.1490. The red dash line represents the V_{LSR} of N_2H^+ line. Contour levels are 30%, 40%...90% of the center peak emissions. The angular resolution of the ATLASGAL survey is indicated by the green circle shown in the lower right corner.

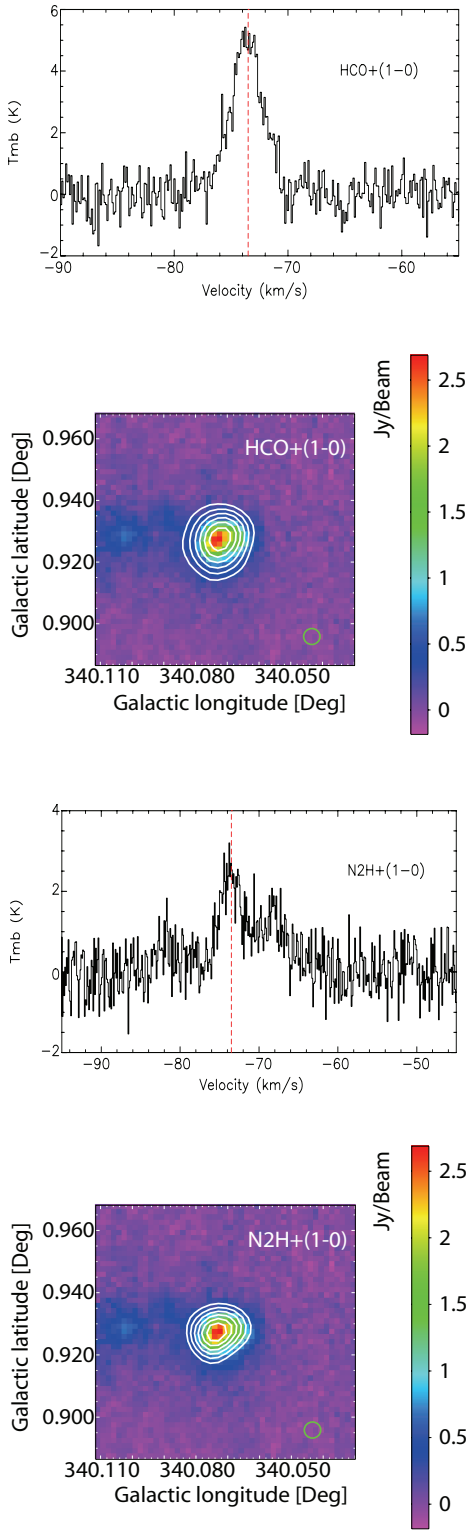

Figure 14. Spectra and integrated intensities superimposed on the 870 μm map in gray scale of G340.0708+00.9267. The red dash line represents the V_{LSR} of N_2H^+ line. Contour levels are 30%, 40%...90% of the center peak emissions. The angular resolution of the ATLASGAL survey is indicated by the green circle shown in the lower right corner.

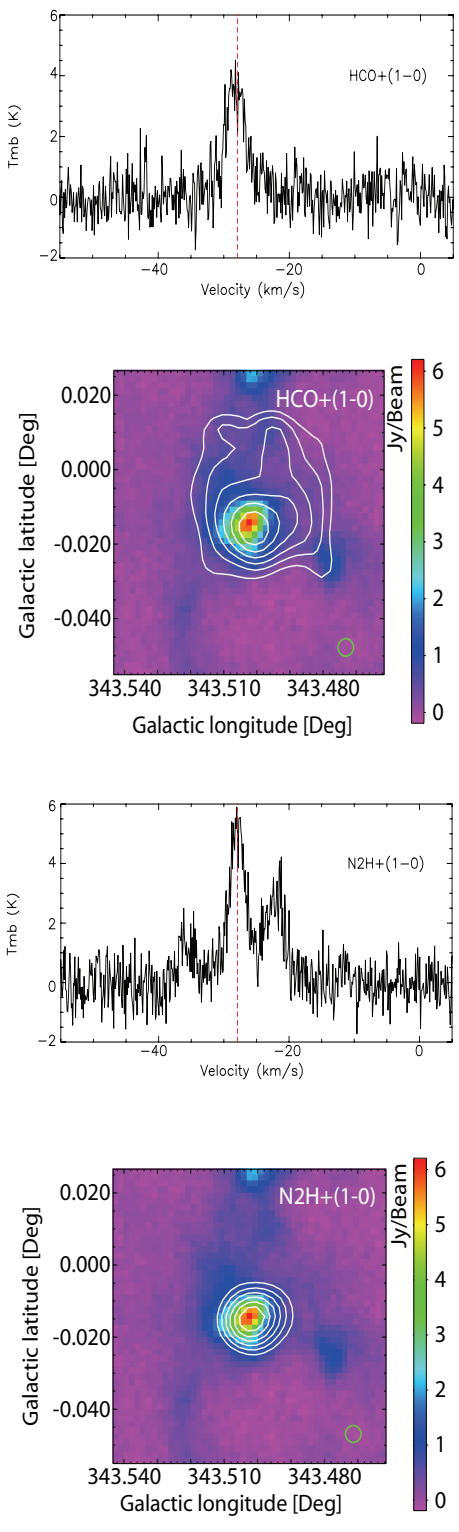

Figure 15. Spectra and integrated intensities superimposed on the 870 μm map in gray scale of G343.5024-00.0145. The red dash line represents the V_{LSR} of N_2H^+ line. Contour levels are 30%, 40%...90% of the center peak emissions. The angular resolution of the ATLASGAL survey is indicated by the green circle shown in the lower right corner.

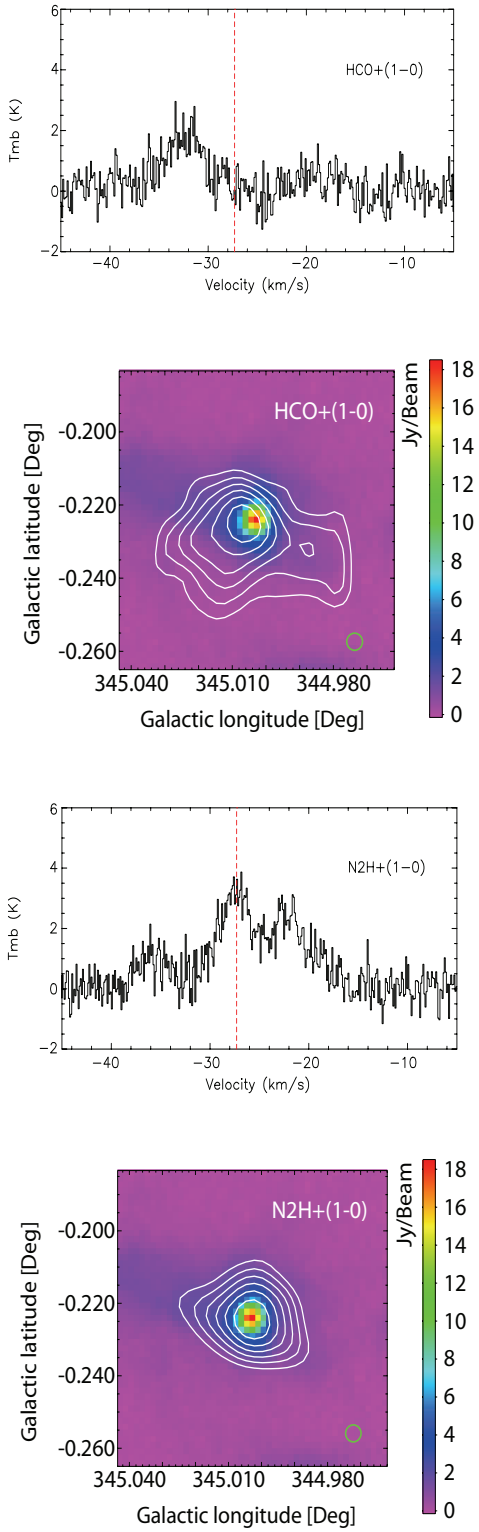

Figure 16. Spectra and integrated intensities superimposed on the 870 μm map in gray scale of G345.0034-00.2240A. The red dash line represents the V_{LSR} of N_2H^+ line. Contour levels are 30%, 40%...90% of the center peak emissions. The angular resolution of the ATLASGAL survey is indicated by the green circle shown in the lower right corner.

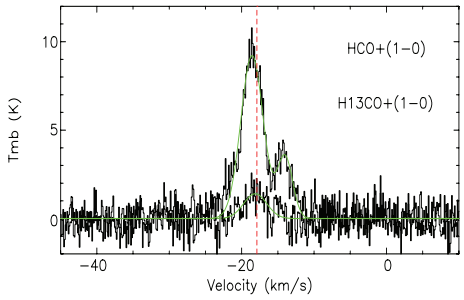

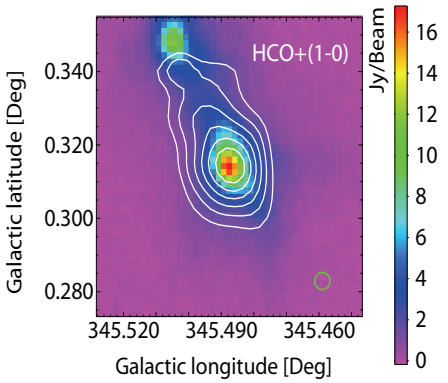

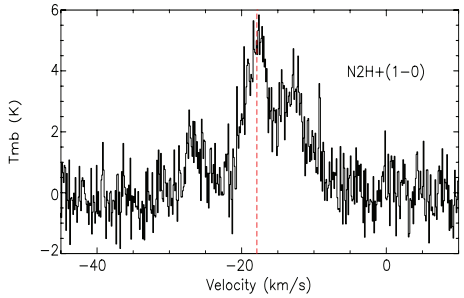

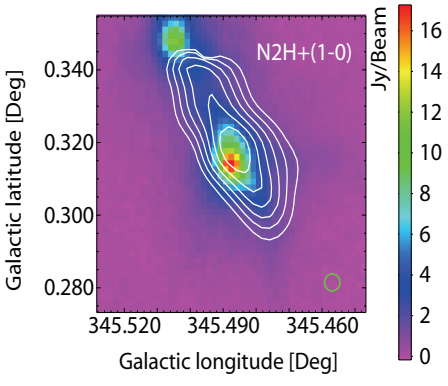

Figure 17. Spectra and integrated intensities superimposed on the 870 μm map in gray scale of G345.4881+00.3148. The red dash line represents the V_{LSR} of N_2H^+ line. The fits of the Myers model are shown with green lines. Contour levels are 30%, 40%...90% of the center peak emissions. The angular resolution of the ATLASGAL survey is indicated by the green circle shown in the lower right corner.

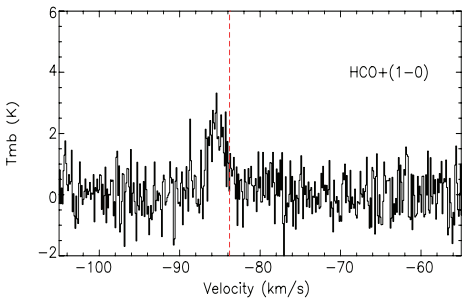

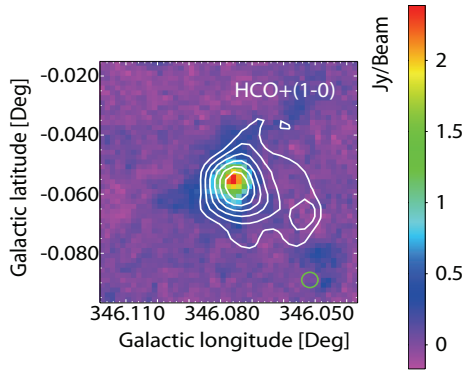

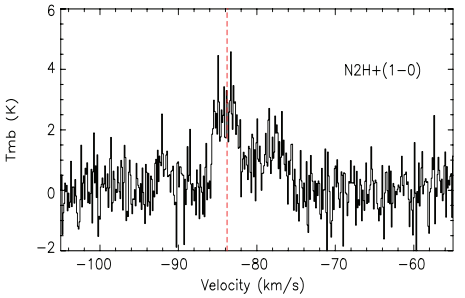

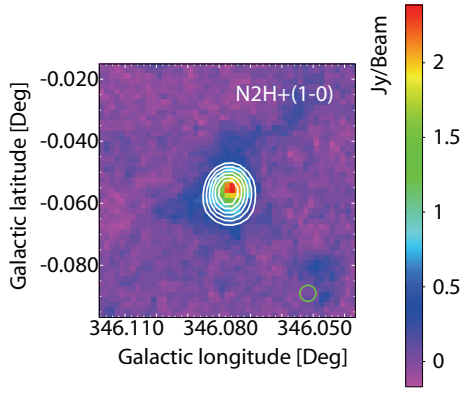

Figure 18. Spectra and integrated intensities superimposed on the 870 μm map in gray scale of G346.0774-00.0562. The red dash line represents the V_{LSR} of N_2H^+ line. Contour levels are 30%, 40%...90% of the center peak emissions. The angular resolution of the ATLASGAL survey is indicated by the green circle shown in the lower right corner.

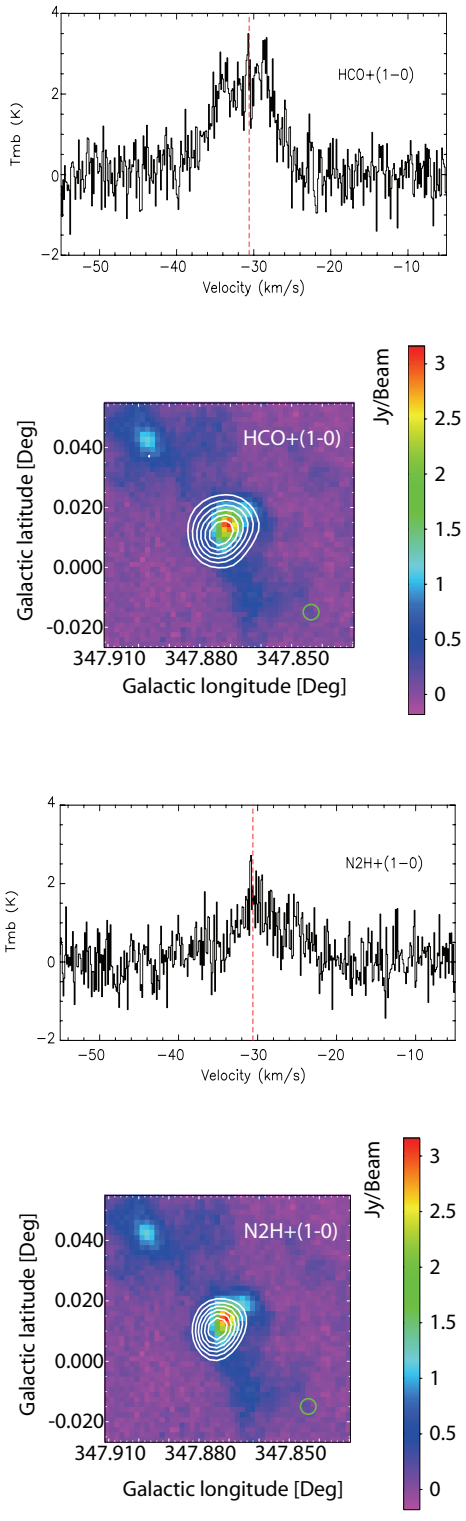

Figure 19. Spectra and integrated intensities superimposed on the 870 μm map in gray scale of G347.8707+00.0146. The red dash line represents the V_{LSR} of N_2H^+ line. Contour levels are 30%, 40%...90% of the center peak emissions. The angular resolution of the ATLASGAL survey is indicated by the green circle shown in the lower right corner.

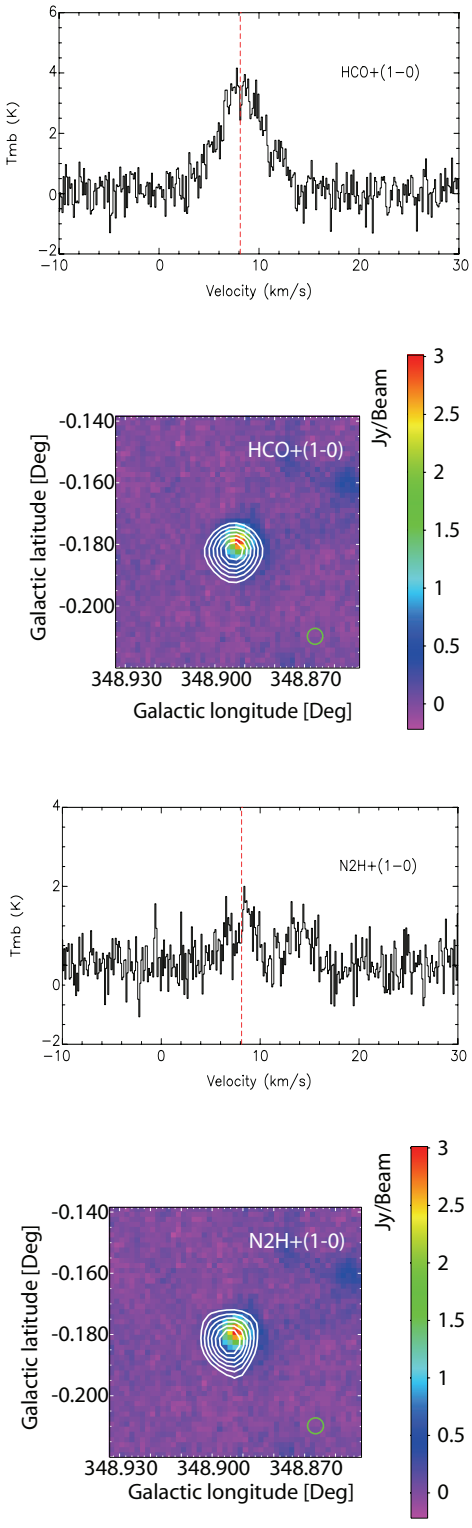

Figure 20. Spectra and integrated intensities superimposed on the 870 μm map in gray scale of G348.8922-00.1787. The red dash line represents the V_{LSR} of N_2H^+ line. Contour levels are 30%, 40%...90% of the center peak emissions. The angular resolution of the ATLASGAL survey is indicated by the green circle shown in the lower right corner.